Surfaces and Interfaces 42 (2023) 103478

Contents lists available at ScienceDirect

Surfaces and Interfaces

journal homepage: www.sciencedirect.com/journal/surfaces-and-interfaces

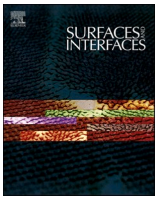

Anchoring self-assembled monolayer at perovskite/hole collector interface for wide bandgap Sn-based solar cells with a record efficiency over 12%

SungWon Cho [a,1], Padmini Pandey [a,b,1], Saemon Yoon [a], Jun Ryu [a], Dong-Gun Lee [a], Qing Shen [c], Shuzi Hayase [c], Hochan Song [d], Hyosung Choi [d], Hyungju Ahn [e], Chang-Mok Oh [f], In-Wook Hwang [f], Jung Sang Cho [g,**], Dong-Won Kang [a,b,*]

[a] *Department of Smart Cities, Chung-Ang University, 84 Heukseok-ro, Dongjak-gu, Seoul 06974, Republic of Korea*
[b] *Department of Energy Systems Engineering, Chung-Ang University, 84 Heukseok-ro, Dongjak-gu, Seoul 06974, Republic of Korea*
[c] *Info-Powered Energy System Research Center, The University of Electro-Communications, 1-5-1 Chofugaoka, Chofu, Tokyo 182-8585, Japan*
[d] *Department of Chemistry, Research Institute for Convergence of Basic Science, and Research Institute for Natural Sciences, Hanyang University, 222, Wangsimni-ro, Seongdong-gu, Seoul 04763, Republic of Korea*
[e] *Pohang Accelerator Laboratory, POSTECH, Pohang 37673, Republic of Korea*
[f] *Advanced Photonics Research Institute, Gwangju Institute of Science and Technology, Gwangju, Republic of Korea*
[g] *Department of Engineering Chemistry, Chungbuk National University, 1 Chungdae-Ro, Seowon-Gu, Cheongju-si, Chungbuk 361-763, Republic of Korea*

ARTICLE INFO

Keywords:
Wide bandgap
Sn-perovskite
Self-assembled monolayers
MeO-2PACz
Hole extraction

ABSTRACT

In perovskite solar cells (PSCs), surface and interfacial conditions play a crucial role in determining overall device performance. In typical p-i-n architecture of wide bandgap (WBG, 1.6–1.8 eV) Sn-based PSCs, the interface between hole transport layer (HTL) and perovskite (PVK) has a significant impact on hole transport, interfacial chemical interactions, and perovskite film quality. This study aims to address these issues by incorporating self-assembled monolayers (SAMs) MeO-2PACz and 2PACz at the PEDOT:PSS HTL/Sn-PVK interface. X-ray photoelectron spectroscopy confirmed the interaction between the anchoring group (P-O^-) of the SAM and S^+ in PEDOT:PSS through phosphonic acid deprotonation at the interface, and improved work function was observed through the UPS study. Furthermore, the SAMs contributed to the formation of a compact PVK film with enhanced preferential orientation. Interestingly, a chemical interaction between the oxygen-donor of the methoxy (CH_3O^-) terminal group in MeO-2PACz and the Sn-halide octahedra was observed, which partly contributed to suppress the oxidation of Sn^{2+} state and defect density of perovskite. Additionally, femtosecond transient absorption spectroscopy (fs-TAS) showed faster trap filling (τ_1) characteristics (τ_1~19 ps). Fs-TAS and photoluminescence further indicated fast hole extraction (τ_2~125 ps) as well as high quenching efficiency of 47%. Based on these findings, an unprecedented efficiency of η~12.16% (certified 11.60%) was achieved in WBG Sn-PSCs using the HTL/MeO-2PACz/PVK structure, outperforming the HTL/2PACz/PVK (8.78%) and HTL/PVK (7.44%) structures. This study provides crucial guidelines on interfacial engineering for WBG Sn-PSCs.

1. Introduction

Metal halide perovskites (PVKs) possess remarkable optoelectronic properties, are easy to process, and exhibit desirable tunability in bandgaps. With tremendous properties halide PVKs have been used in various applications such as LEDs, energy storage devices, and particularly as efficient photo-absorber in perovskite solar cells (PSCs) with a certified power conversion efficiency (PCE) of 25.8% [1]. However, typical PSCs, consisting of photo-absorbers with specific bandgaps, have limited optical absorption. This limitation has driven the development of tandem solar cells (TSCs) with multiple light harvesters of different bandgap combinations [2]. Commercializing TSCs can be challenging due to the presence of toxic lead (Pb) in halide PSCs, which falls under hazardous materials regulations [3]. As a result, pure tin (Sn)-based PSCs have emerged as promising next-generation PSCs due to several benefits, including high carrier mobility and high theoretical PCE.

---

* Corresponding author at: Department of Energy Systems Engineering, Chung-Ang University, 84 Heukseok-ro, Dongjak-gu, Seoul 06974, Republic of Korea.
** Corresponding author.
E-mail addresses: jscho@cbnu.ac.kr (J.S. Cho), kangdwn@cau.ac.kr (D.-W. Kang).

[1] Contributed equally.

https://doi.org/10.1016/j.surfin.2023.103478
Received 5 July 2023; Received in revised form 7 September 2023; Accepted 29 September 2023

However, Sn-based PSCs suffer from structural and operational instability. Despite continuous efforts to enhance PCE in Sn-PSCs (with a bandgap of approximately 1.43 eV), it reaches only around 14.8% [4], making it suitable as the bottom sub-cell in PVK TSCs. To develop Pb-free all-PVK TSCs, it is equally important to conduct an in-depth study to develop Sn-based wide bandgap (WBG, 1.6–1.9 eV) PSCs as top sub-cells, which can enhance the open circuit voltage (V_{oc}) in TSCs [5]. In our previous report, we adopted a compositional engineering strategy in WBG Sn-PVK and achieved a decent PCE of 7.9% [6]. However, optimizing the device performance goes beyond surface and bulk optimization of the PVK layer and charge transport layer (CTL). The CTL/PVK interface plays an important role in efficient photovoltaic (PV) operation; therefore, interfacial engineering is vital to enhance device performance. Conventionally, poly(3,4-ethylenedioxythiophene): poly (styrenesulfonate) (PEDOT:PSS) has been widely used as a hole transport layer (HTL) in WBG Sn-PSCs [7–10]. It significantly affects hole transport dynamics due to energy level stiffness and chemical interactions at the perovskite/HTL interface, thereby influencing the quality of perovskite film [8,11].

Introducing self-assembled monolayer (SAM) on top of the HTL is known as an effective approach to mitigate moisture infiltration from PEDOT:PSS, thereby protecting the degradation of PVK and modify the work function of HTL [8,12,13]. SAMs are ultra-thin 2D nanostructures composed of spacer molecules such as carbazole, with anchoring (carboxylic, phosphonic, and boronic acids) and terminal head groups [14–17]. Replacing PTAA with either 2PACz or MeO-2PACz substantially increases the device efficiency of Pb-PSCs (PCE∼20.8%) due to the high hole selectivity of both 2PACz and MeO-2PACz [18]. In Sn-PSCs, 2PACz as an interlayer over PEDOT:PSS demonstrated 8.6% PCE, attributed to improved device performance through better HTL/PVK interface alignment achieved by through work function tuning [8]. Although previous studies have implemented SAMs, specifically 2PACz or MeO-2PACz, in PSCs to tune work function (WF) and adjust band alignments, these SAM layers differ in their terminal functionality and their effects on device performance. However, no clear guidelines are available to differentiate and determine the optimal choice of SAMs when dealing with Sn-PSCs.

To explore the multiple functionalities of SAMs as interlayers between HTL and Sn-PVK interface, this study conducts a comparative analysis of utilizing 2PACz and MeO-2PACz. The aim is to provide a comprehensive guideline for selecting the appropriate SAM to enhance device performance in WBG Sn-PSCs. The comparative analysis includes HTL/PVK, HTL/2PACz/PVK, and HTL/MeO-2PACz/PVK, where HTL refers to PEDOT:PSS (HTL) and PVK refers to WBG Sn-PVK ($PEA_{0.15}FA_{0.75}MA_{0.10}SnI_2Br$). The results showed an enhancement in device performance from 7.44 to 8.78% using HTL/2PACz/PVK. Interestingly, the PCE further increased to 12.16% (with a certified PCE of 11.60%) for HTL/MeO-2PACz/PVK, setting a record PCE among WBG (1.6–1.8 eV) Sn-PSCs reported to date. X-ray photoelectron spectroscopy (XPS) revealed the interaction of $P\text{-}O^-$group (anchoring phosphonic acid group) of SAM with S^+ in PEDOT:PSS, resulting in an improved work function at the HTL as observed through ultraviolet photoelectron spectroscopy (UPS). The XRD analysis indicated a preferred orientation of crystallographic planes for HTL/MeO-2PACz/PVK, and the interaction between Sn halide octahedra and the methoxy group led to suppressed non-radiative recombination and controlled oxidation of perovskite film. Detailed analysis of hole extraction dynamics demonstrated fast trap filling and efficient hole extraction in HTL/MeO-2PACz/PVK. Furthermore, the device performance of HTL/MeO-2PACz/PVK structure exhibited almost 100% retention of its initial efficiency in long-term stability (under N_2-filled glovebox conditions) over 2000 hrs, with 92.6% performance retention observed over 300 hrs (device measured at ambient atmospheric conditions with relative humidity (RH) of 30–50%). In contrast, HTL/2PACz/PVK and HTL/PVK devices degraded and retained only 72.1% and 74.9% of initial performance, respectively. The significant findings and fundamental insights from this work provide valuable guidelines for choosing the most suitable SAMs with specific head and anchoring group functionalities as interlayers, that can help in multiple ways to passivate perovskite defects, improve work function, and hole extraction rate, which collectively enhances the device performance and useful for eco-friendly WBG Sn-PSCs and all-PVK tandem solar cells.

2. Results and discussion

To investigate the impact of SAM interlayer on the optoelectronic properties of WBG Sn-PSCs, we initially fabricated p-i-n device structures. The device architecture consisted of ITO/HTL (PEDOT:PSS)/SAM/WBG-PVK ($PEA_{0.15}FA_{0.75}MA_{0.10}SnI_2Br$)/PCBM/BCP/Ag, as illustrated in Fig. 1(a). SAM treatments were applied to the HTL/PVK interfaces. The experimental section provides detailed information about the material processing and device fabrication, along with the characterization tools used. The current density-voltage curves and comprehensive photovoltaic (PV) parameters with forward and reverse scans are presented in Fig. 1(b) and Table S1, respectively. We observed a power conversion efficiency (PCE) of 7.44% for the control PSC with HTL/PVK. However, the introduction of 2PACz (HTL/2PACz/PVK) led to a slight improvement in the PV performance, resulting in a PCE of 8.78%. Notably, a significant enhancement in device performance was achieved by incorporating MeO-2PACz (HTL/MeO-2PACz/PVK), yielding a remarkable PCE of 12.16% (certified PCE of 11.60% in Fig. S2), accompanied by a V_{oc} of 0.93 V and J_{sc} of 16.60 $mA\cdot cm^{-2}$ and reduced hysteresis as indicated in Table S1. This PCE surpasses the previous record performance (11.17%) reported to date for WBG Sn-PSCs (>1.6 eV), as indicated in Fig. S1 [7].

We conducted a series of tests on 15 devices for each case, and the statistical distribution of all device parameters is presented in Fig. S3. The stabilized power output (SPO) at maximum power point (MPP) illuminated under 1 Sun in ambient atmospheric conditions for HTL/MeO-2PACz/PVK is shown in Fig. S4. To gain a better understanding of significant enhancement in device efficiency, we performed external quantum efficiency (EQE), internal quantum efficiency (IQE) measurements, electrochemical impedance spectroscopy (EIS), and dark J-V measurements. The champion device (HTL/MeO-2PACz/PVK) exhibited an increase in EQE, IQE, and integrated J_{sc} (15.87 $mA\cdot cm^{-2}$), consistent with the J_{sc} value obtained from the J-V characteristics (Figs. S5, S6). The enhancement in quantum efficiency is typically attributed to efficient charge carrier separation/collection and improved light absorption. In this case, we speculate that the increase in EQE could be mainly ascribed to efficient charge carrier collection from improved energy band alignment (favorably tuned work function) as well as improved PVK film quality, with reduced defect states and enhanced photogenerated charge carrier separation [6]. IQE measurements also revealed enhanced internal charge collection efficiency by employing the SAMs addition between HTL/PVK interface, especially in case of MeO-2PACz.

The film morphology was characterized using field emission scanning electron microscopes (FESEM), as detailed in the characterization section. The FESEM image of HTL/PVK (Fig. S7(a)) shows the presence of highly smooth PVK film with certain pinholes observed at the surface. It is expected that 2D halide perovskite randomly distributed on the surface and hence grain boundaries were not easily detected at the surface. Because a solution processed polycrystalline perovskite film (Glass/ITO/PEDOT:PSS/perovskite) could not be formed without any grain boundary, its polycrystalline nature with obvious some grain boundaries can be observed through the FESEM cross-sectional image as shown in Figure S8. In the case of HTL/2PACz/PVK (Figure S7(b)), a few pinholes were detected between PEDOT:PSS and PVK. However, for HTL/MeO-2PACz/PVK (Figure S7(c)), we observed a high-quality PVK film without pinholes. This could be attributed to the chemical interaction between the methoxy terminal group of MeO-2PACz and Sn-PVK [19]. Direct contact between the Sn-PVK layer and acidic PEDOT:PSS

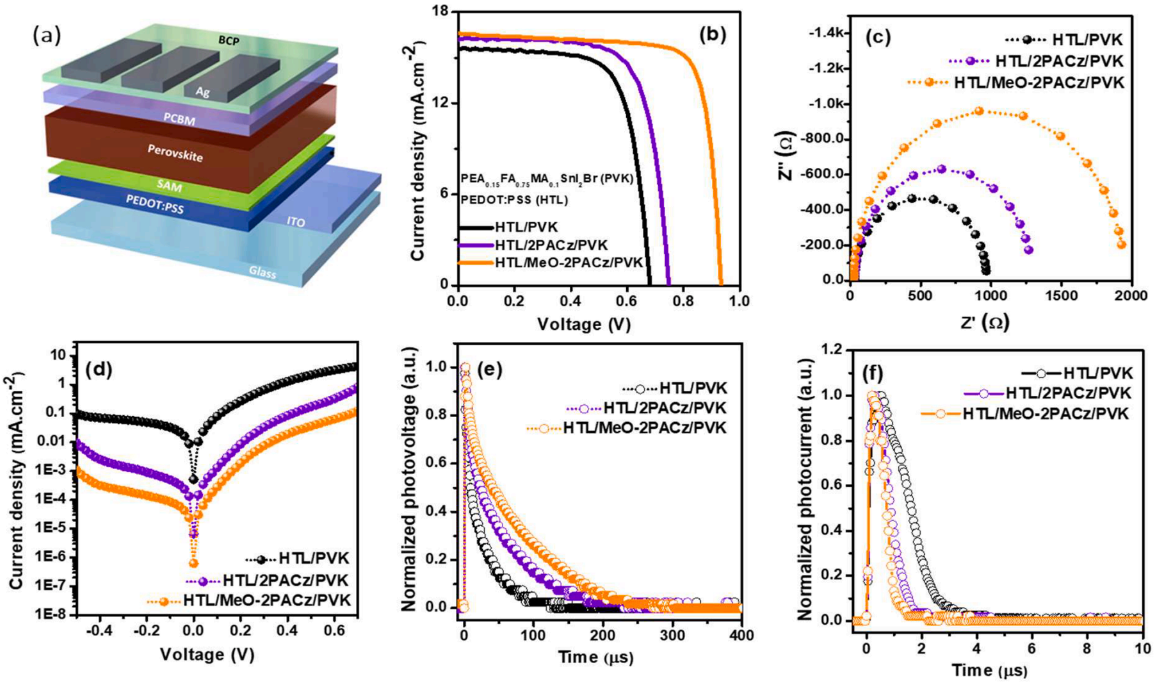

Fig. 1. (a) Schematic of p-i-n device structure, (b) Current-Voltage (J-V) curves, (c) Nyquist plots (d) Dark J-V (e) TPV and (h) TPC plots for HTL/PVK, HTL/2PACz/PVK and HTL/MeO-2PACz/PVK.

can lead to undesirable degradation of PVK, however by preventing the direct interaction of Sn-PVK with PEDOT:PSS, such degradation can be controlled [8,12]. EIS measurements were conducted in the frequency range of 2 kHz to 1 MHz at 0.65 V for all three cases (Fig. 1(c)). The data were fitted into an equivalent circuit with series resistance (R_s) and recombination resistance (R_{rec}) (Figure S9). R_{rec} showed a significant improvement from 964.08 Ω (HTL/PVK) to 1268.66 Ω (HTL/2PACz/PVK). Furthermore, we observed an even greater enhancement in R_{rec}, reaching 1929.02 Ω for the HTL/MeO-2PACz/PVK device, resulting due to improved interfacial connectivity at HTL/PVK interface and responsible for an increase in the fill factor (FF) [20]. The HTL/MeO-2PACz/PVK device has the highest R_{rec} of 1929.02 Ω, we may speculate that the improved V_{oc} in HTL/MeO-2PACz/PVK device is resulted due to suppressed non-radiative recombinations. Fig. 1(d) displays the dark J-V characteristic curves for the HTL/PVK, HTL/2PACz/PVK, and HTL/MeO-2PACz/PVK samples. The current density level is lower for the HTL/MeO-2PACz/PVK structure compared to the HTL/PVK and HTL/2PACz/PVK cases, indicating minimal leakage current when using the MeO-2PACz SAM. This suggests a significantly reduced trap density in the PVK film of the HTL/MeO-2PACz/PVK device, which aligns with the enhanced R_{rec} observed in the EIS analysis [21,22].

To further validate our observations regarding the reduced trap densities in the HTL/MeO-2PACz/PVK architecture compared to HTL/2PACz/PVK and HTL/PVK-based devices, we performed Mott-Schottky (M-S) analysis using capacitance-voltage (C-V) measurements. The M-S equation, $1/C^2 = 2(V_{bi}-V)/(A^2 q\varepsilon\varepsilon_0 N_d)$ [23,24], was employed, where C, V, A, q, ε_0, and ε represent the capacitance, applied bias, active area (0.04 cm^2), elementary charge, permittivity of free space, and static permittivity of PVK, respectively. The V_{bi} (built-in potential) and N_d (defect density) were determined from the X-axis intercept and slope of the linear portion of the M-S curve (Figure S10). The HTL/MeO-2PACz/PVK device exhibited an improved V_{bi} of approximately 0.444 V, compared to HTL/2PACz/PVK (0.409 V) and HTL/PVK (0.367 V) counterparts. This suggests better separation of photo-generated carriers and a more favorable driving force in extended depletion regions [25]. The calculated N_d values were 1.32×10^{11}, 1.01×10^{11}, and 7.77×10^{10} cm^{-3} for HTL/PVK, HTL/2PACz/PVK, and HTL/MeO-2PACz/PVK samples, respectively. This indicates that the incorporation of MeO-2PACz as the interfacial SAM at HTL/PVK effectively inhibits the trap density in Sn-PVK. To assess the impact of the SAM on charge collection processes, transient photovoltage (TPV) and photocurrent (TPC) measurements were conducted (Fig. 1(e, f)). The carrier recombination lifetime (τ_{rec}) and charge carrier transport lifetime (τ_{ct}) were extracted from the fitted curves using Eq. (1). The HTL/PVK and HTL/2PACz/PVK PSCs exhibited τ_{rec} (τ_{ct}) values of approximately 32.51 μs (1.17 μs) and 61.97 μs (0.61 μs), respectively. While comparatively slow carrier recombination lifetime ($\tau_{rec} \sim 85.88$ μs) and carrier transport rate ($\tau_{ct} \sim 0.29$ μs) were observed, observed in HTL/MeO-2PACz/PVK which shows that the MeO-2PACz SAM interlayer beneficially reduced defects at the HTL/PVK interface and within the bulk of the PVK.

To clarify these observations, we conducted detailed crystallographic analyses using XRD measurement as shown in Fig. 2(a). The major XRD peaks at 14.1°, and 28.4°, with no other impurities observed in HTL/PVK, HTL/2PACz/PVK, and HTL/MeO-2PACz/PVK films, correspond to (100) and (200) crystallographic planes of PVK [6], indicating a preferential crystal orientation. The XRD peak intensity was enhanced in the HTL/2PACz/PVK film and further increased in the HTL/MeO-2PACz/PVK sample, suggesting that the SAM interlayer could improve the crystallinity and preferred orientation of PVK [26]. Moreover, the full width at half maxima (FWHM) was extracted from the XRD patterns [27]. It was confirmed that the FWHM values decrease successively HTL/PVK, HTL/2PACz/PVK, and HTL/MeO-2PACz/PVK, provided in Table S2. As reported, wet surfaces generally have higher tension-dragging forces [28]. PEDOT:PSS, for instance, exhibits high surface tension dragging force, which reduces the mobility of PVK film growth along grain boundaries. However, surface treatment of PEDOT:PSS with SAM dramatically decreases the surface tension dragging forces, potentially leading to the formation of larger-grain PVK films. To further investigate these findings, we performed grazing-incidence wide-angle X-ray scattering (GIWAXS). Fig. 2(b–d) depict the 2D GIWAXS images for HTL/PVK, HTL/2PACz/PVK, and HTL/MeO-2PACz/PVK films on an ITO substrate at an incident angle of

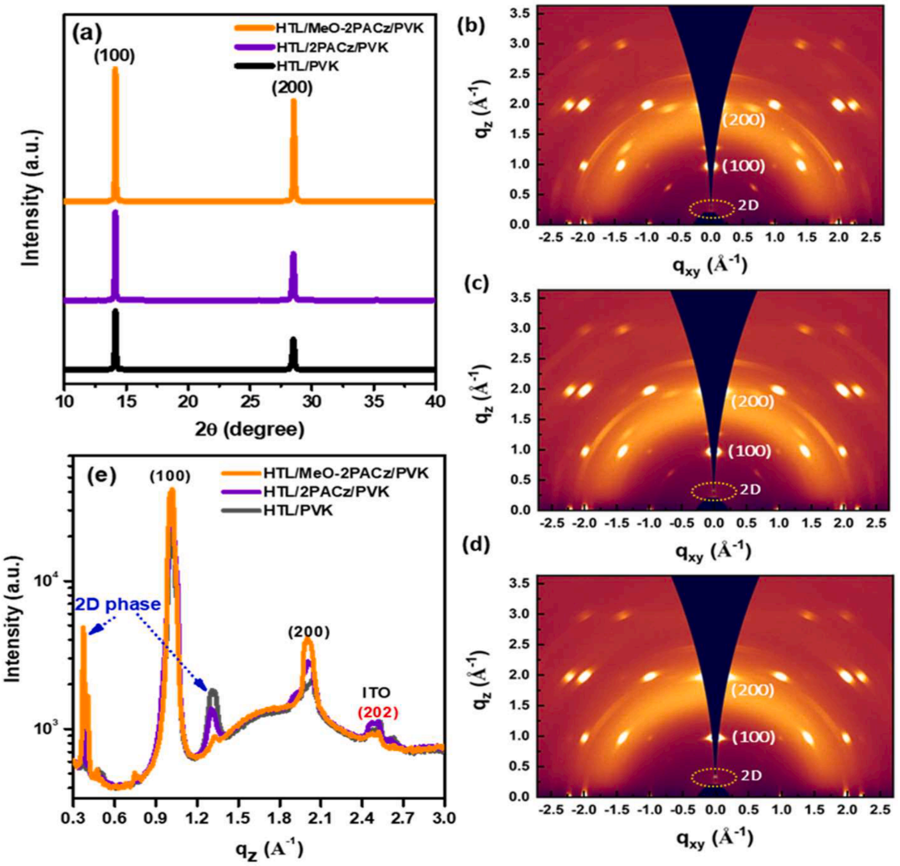

Fig. 2. (a) X-ray diffraction (XRD) patterns and (b-e) Comparative Grazing-incidence wide-angle X-ray scattering (GIWAXS) and line cut profile from GIWAXS images of HTL/PVK, HTL/2PACz/PVK, and HTL/MeO-2PACz/PVK.

0.12°. The corresponding line cut profile is shown in Fig. 2(e), and additional instrument and parameter details are provided in the characterization section. The 2D GIWAXS patterns (Fig. 2(b)) exhibit Bragg spots for HTL/PVK, where the Bragg spots located at $q_z\sim1.0\ \mathring{A}^{-1}$ and $q_z\sim2\ \mathring{A}^{-1}$ along q_z direction correspond to the preferential growth of PVK crystals on the (100) and (200) *hkl* planes. It was further observed that, the intensity of Bragg spots slightly increased for HTL/2PACz/PVK (Fig. 2(c)) and intensified more for HTL/MeO-2PACz/PVK (Fig. 2(d)) than other ones. Fig. 2(e) presents the line cut profile of the HTL/PVK, HTL/2PACz/PVK, and HTL/MeO-2PACz/PVK structures, indicating the preferred orientation at the (100) and (200) planes with highly prominent peak intensities in the HTL/MeO-2PACz/PVK sample. With these results, we may speculate that the insertion of SAM as interlayer benefits to improve the crystallinity of PVK and helps in preferred growth orientation, which is consistent with the XRD analysis.

To confirm the presence of the SAM at the HTL/PVK interface and

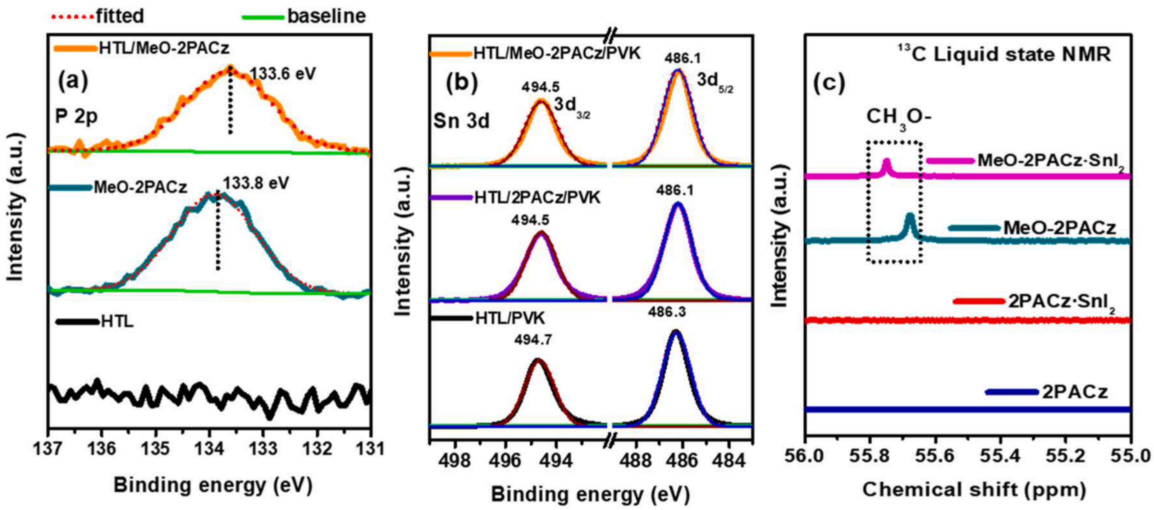

Fig. 3. Comparative X-ray photoelectron spectroscopy (XPS) core spectra (a) P 2p XPS core spectra for PEDOT:PSS (HTL) (black line), MeO-2PACz (green line) and HTL/MeO-2PACz (orange line) (b) Sn 3d XPS spectra for HTL/PVK, HTL/2PACz/PVK, and HTL/MeO-2PACz/PVK, respectively. (c) ^{13}C Nuclear magnetic resonance (NMR) spectra of 2PACz, 2PACz·SnI$_2$, MeO-2PACz, and MeO-2PACz·SnI$_2$ in DMSO-d$_6$ solution.

investigate the interactions between HTL/SAM and SAM/PVK, surface chemical analysis was conducted using XPS measurement. The XPS core spectra shown in Fig. 3 (a, b) and Figure S11 were calibrated with the C1s adventitious carbon peak at binding energy (BE) of 284.6 eV [29]. As shown in Figs. S11 and 3(a), the XPS core spectra of the S 2p and P 2p peaks indicate the presence of PEDOT:PSS (HTL) and MeO-2PACz (SAM) layers. In the case of HTL and HTL/MeO-2PACz (Figure S9), the S 2p core spectra exhibit distinct peaks in the BE range of 163–166 eV and 168–170 eV. The thiophene component of PEDOT is fitted in HTL and HTL/MeO-2PACz, showing a spin-orbit doublet at 163.8 eV ($2P_{3/2}$) and 165.0 eV ($2P_{1/2}$), with a splitting of 1.2 eV as expected for S 2p state. The contribution of styrene sulfonate (SS) component of PSS to the S 2p peak appears at 168.3 eV ($2P_{3/2}$) and 169.4 eV ($2P_{1/2}$) BEs [30,31]. Furthermore, the interaction of MeO-2PACz with PEDOT:PSS was identified through the P 2p XPS core spectra as depicted in Fig. 3(a). The XPS signal was observed in MeO-2PACz and HTL/MeO-2PACz films, indicating the presence of MeO-2PACz (SAM) at PEDOT:PSS surface. In the HTL/MeO-2PACz film, a shift towards lower binding energy (133.6 eV) in the P 2p (Fig. 3(a)) was observed. The shift is possibly due to the deprotonation of the phosphonic acid terminal group upon binding to the surface and corresponds to the interaction of P-O^- of MeO-2PACz with S^+ atoms in PEDOT [8,32–34]. UPS was further conducted to examine the difference in work function (WF) of HTL/SAM with HTL (PEDOT:PSS). The UPS measurement was performed using an ITO substrate for all cases and the instrumental information is provided in the characterization details. Figure S12 shows the secondary energy cutoff region used to calculate the WF ‘ϕ’, which was determined to be 5.21 eV for ITO/HTL [35]. A slight increase in WF values was observed for ITO/HTL/SAM films, with values of 5.25 eV for ITO/HTL/2PACz and 5.30 eV for ITO/HTL/MeO-2PACz, as an approximate estimation. It is noteworthy that the increase in the WF of the ITO/HTL/MeO-2PACz sample indicates more promising energetics as a hole transport layer in our device.

We conducted an extended XPS study to investigate the interactions between SAM and PVK layers. A complete survey scan of HTL/MeO-2PACz/PVK and HTL/2PACz/PVK, compared to HTL/PVK film, is shown in Fig. S13. The graph indicates the presence of Sn 3d, I 3d, Br 3d, C 1 s, N 1 s, and O 1 s peaks as marked. To examine the chemical state variation resulting from the interaction between SAM with Sn-PVK, XPS core spectra of C 1 s, Sn 3d, and I 3d were analyzed. The C 1 s core spectra for HTL/PVK, HTL/2PACz/PVK, and HTL/MeO-2PACz/PVK were deconvoluted as shown in Fig. S14(a). To determine the contribution of PVK, an additional C 1 s core spectrum of $PEA_{0.15}FA_{0.75}MA_{0.10}SnI_2Br$ PVK is presented in Fig. S14 (b). For PVK, the XPS core spectrum was deconvoluted into four peaks. The peak at 285.5 eV is attributed to the C—N signal from MA [36]. The BE~287.8 eV corresponds to the $C{=}NH_2^+$ component of FA, while BE~288.7 eV is ascribed to the surficial interaction with moisture (C = O) [29,37]. In Figure S14 (a), the C 1 s core spectra show the coexistence of FA, MA, and PEA components of PVK, SAM interlayer, and PEDOT:PSS layer. The peak at 286.3 eV corresponds to the coexistence of C-S/C—O and C—N components of PEDOT:PSS, 2PACz, or MeO-2PACz and PEA (from PVK) in films [38,39]. Notably, BE peak at 287.6 eV in HTL/2PACz/PVK and HTL/MeO-2PACz/PVK corresponds to the C-P component from MeO-2PACz or 2PACz SAM interlayer [18], which is absent in the C 1 s spectrum of HTL/PVK. We further examined Sn 3d and I 3d XPS spectra (Figs. 3(b) and S15) to verify the oxidation states and chemical interaction of PVK with SAM interlayers. The BEs of Sn $3d_{5/2}$ (Sn $3d_{3/2}$) for HTL/PVK are at 486.3 eV (494.7 eV), corresponding to the Sn^{2+} state, as previously reported [40,41]. The signature peaks of I $3d_{5/2}$ (I $3d_{3/2}$) are located at 618.8 eV (630.4 eV). A small shift (~0.2 eV) towards lower BEs in the Sn 3d and I 3d spectra (Figs. 3(b) and S15) was observed for both HTL/2PACz/PVK and HTL/MeO-2PACz/PVK, compared to pristine HTL/PVK, may associated to chemical interaction between Sn-PVK and SAM interlayer [42,43]. The XPS analysis of HTL/2PACz/PVK and HTL/MeO-2PACz/PVK films suggest certain chemical interactions. However, MeO-2PACz differs from 2PACz due to the presence of an additional terminal methoxy group (CH_3O^-). Based on the results obtained from the device study and crystallographic analysis, it is evident that MeO-2PACz has additional advantages over 2PACz, which may be attributed to the existence of an additional CH_3O^- terminal group in MeO-2PACz.

To provide stronger evidence for the hypothesis of PVK interaction with the methoxy terminal group of MeO-2PACz, we performed ^{13}C liquid state nuclear magnetic resonance (NMR) measurements on samples containing 2PACz, 2PACz·SnI_2 MeO-2PACz, and MeO-2PACz·SnI_2 in deuterated DMSO-d_6 solution as shown in Fig. 3(c) and Fig. S16 (sample preparation details are provided in characterization section). The resonance signal at 39.52 ppm (Fig. S16) corresponds to the d_6 solution, as reported [44]. The resonance signals obtained from the NMR study are in good agreement with the ^{13}C NMR of 2PACz and MeO-2PACz (provided in supporting information, Fig. S16) [18]. No chemical shift is observed in the ^{13}C NMR spectrum of 2PACz·SnI_2 as compared to 2PACz. In Fig. 3(c), the resonance signal at 55.68 ppm in MeO-2PACz corresponds to the carbon of the methoxy (CH_3O^-) terminal group of MeO-2PACz, which exhibits a chemical shift to 55.75 ppm for MeO-2PACz·SnI_2. Studies on the interaction of PVK with valeric acid using Fourier Transform Infrared Spectroscopy (FT-IR) and NMR spectroscopy analysis have revealed a strong electrostatic interaction between O and Sn^{2+} (HO—C = O—Sn^{2+}) [45]. Electrostatic interaction between the O^-donor from the CH_3O^- a group of 4-methoxyphenylacetic acid and anisole with PVK has also been observed, suggesting the interaction of the O-donor with the uncoordinated Pb^{2+} in PVK octahedra, as investigated by Zhou et al. [46]. Theoretical investigations also suggest that the most favorable interaction of the CH_3O^- a group of methoxybenzene is with the uncoordinated Pb^{2+} in Pb halide octahedra. Based on the evidence from our NMR analysis and previous reports [40], we speculate that the chemical shift in MeO-2PACz·SnI_2 originates from the chemical interaction between O-donor (CH_3O^- terminal group) and Sn halide octahedra. Sn-PVK, having a higher defect density than Pb-PVK, generates several undercoordinated Sn ions during the fabrication process. From our observation (Fig. 3(c)), the chemical shift in ^{13}C NMR (CH_3O^-) suggests that the O-donor of the MeO-2PACz terminal group combines with undercoordinated Sn ions, thereby helping to suppress the defect density of PVK in the HTL/MeO-2PACz/PVK architecture. These observations are consistent well with the reduction in defect density confirmed by the device characterizations described above.

The charge transfer dynamics at the CTL/PVK interface play a critical role in achieving high performance in PSCs. Several pioneering studies have been conducted to determine the charge extraction processes at HTL/PVK and ETL/PVK interfaces [47–49]. To identify the difference in hole selectivity in HTL/PVK without and with SAM interlayer, we further carried out a study on charge transfer dynamics using steady-state photoluminescence (SS-PL), and femtosecond-transient absorption spectroscopy (fs-TAS). The SS-PL measurement was performed using an excitation wavelength of 470 nm (Fig. S17), compared to the reference glass/PVK film.

The emission peak at 747 nm (PVK) corresponds to $PEA_{0.15}FA_{0.75}MA_{0.10}SnI_2Br$ as reported in our previous work [6]. However, we observed an additional signal at 785 nm in the reference PVK film, which could be attributed to phase segregation in mixed halide PVK [50]. Phase segregation leads to the generation of local bromine and iodine-rich phases, with the iodine-rich phase primarily responsible for hole accumulation. Nevertheless, the phase segregation in mixed halide PVKs can be suppressed by interfacing PVKs with charge extraction layers [51], suggesting that PVK films with charge extraction layers experienced almost no PL spectral signal from the segregated phase. In Fig. S17, the PL quenching for HTL/MeO-2PACz/PVK film is comparably higher than that of HTL/PVK and HTL/2PACz/PVK films. PL quenching efficiency (PLQE) was determined using the following equation: PLQE (%) $= \left[\frac{I_0 - I}{I_0}\right]$x100, where I_0 represents the PL peak intensity of PVK, and I stands for emission intensity from HTL/PVK or HTL/SAM/PVK films [52]. The PLQE extracted for HTL/MeO-2PACz/PVK (approx. 47%) is higher compared to HTL/PVK (approx. 32%) and HTL/2PACz/PVK (approx. 35%), suggesting better hole extraction in HTL/MeO-2PACz/PVK sample.

To further elucidate the origins behind the enhanced performance in HTL/MeO-2PACz/PVK PSC, we conducted fs-TAS measurements to analyze the charge carrier dynamics in HTL/PVK, HTL/2PACz/PVK, and HTL/MeO-2PACz/PVK films. Fig. 4(a–c) presents the fs-TAS results obtained using a photoexcitation wavelength (λ_{pump}) of 650 nm and a pump fluence of 10 μJ·cm^{-2}, with different time delays ranging from 1 to 1000 ps. The measurements were taken within the wavelength range of 500 to 800 nm. The fs-TAS results (Fig. 4(a–c)) exhibited three distinct features. The prominent ground state bleach (GSB) signal observed in the wavelength range of 700–750 nm was identified as photoinduced transient bleach 1 (PIB1), which corresponds to the bandgap (E_g) of PVK (Figure S18). This signal originates from band-to-band transitions between the valance and conduction bands at lower energies. The weak signals observed in the wavelength range of 570–620 nm are assigned as the PIB2 region, which corresponds to transitions involving higher energy states. Additionally, a minor feature in the wavelength range of 630–670 nm corresponded to photo-induced transient absorption (PIA) [53–55]. Since fs-TAS measurements consist of multiple components, where PIB2 and PIA bands (Fig. 4(a–c)) disappear with increasing delay time, we focused on the PIB1 band for further analysis. As a function of optical delay time, the PIB1 signal at 1 ps was centered at 722 nm in all the films. In HTL/PVK, the PIB1 band exhibited a redshift to 724 nm at 100 ps, followed by further shifts to 726 nm (500 ps) and 728 nm (1000 ps). In HTL/2PACz/PVK film, the PIB1 band shifted from 722 nm (1 ps) to 725 nm (100 ps), with an additional redshift of 2 nm observed at 500 ps and 1000 ps. Interestingly, in HTL/MeO-2PACz/PVK film, the PIB1 band shift remained from 722 nm (1 ps) to 727 nm (100 ps) and remained constant throughout the delay time range of 100 ps to 1000 ps.

The early-stage band shift observed may correlate to E_g renormalization. Upon photoexcitation, the presence of free charge carriers tends to renormalize the E_g, resulting in a shift of the density of states. During this process, the generated hot charge carriers occupy new energy states below the band edge, leading to transient absorption (TA) and the appearance of PIA signals, which can be attributed to new transitions [56,57]. Furthermore, the observed peak shift at different delay times in HTL/PVK could be attributed to interfacial defect density states [58]. However, the insertion of MeO-2PACz at the HTL/PVK interface reduces the formation of defect states as mentioned earlier.

The relaxation kinetics of photoinduced transient bleach were probed at 725 nm for different excitation pump fluences ranging from 1 to 10 μJ·cm^{-2}. The corresponding lifetime decay extracted from the tri-exponentially fitted data is shown in Fig. 4(d–f) using the following equation: $y = y_0 + A_1 \exp(-x/\tau_1) + A_2 \exp(-x/\tau_2) + A_3 \exp(-x/\tau_3)$, and the obtained decay parameters are provided in Table S3. At pump fluences of 1, 5, and 10 μJ·cm^{-2}, the fast component designated as (τ_1) exhibited decay times of 134 ps, 73 ps, and 26 ps for HTL/PVK, 104 ps, 56 ps and 22 ps for HTL/2PACz/PVK, 70 ps, 54 ps, and 19 ps for HTL/MeO-2PACz/PVK film. These values indicate a considerably faster decay for the HTL/2PACz/PVK system, which becomes even quicker in the case of the HTL/MeO-2PACz/PVK film. The fast component (τ_1)

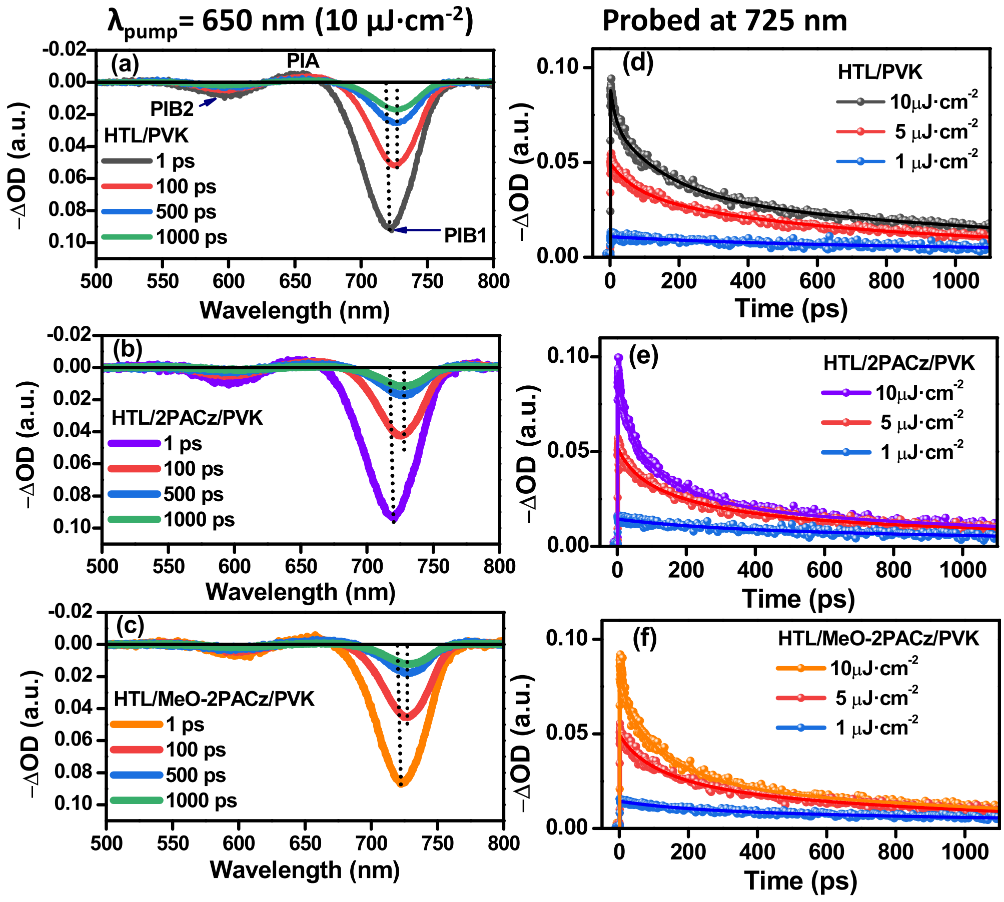

Fig. 4. Femtosecond-TAS (a-c) ΔOD as a function of wavelength at various time delays using a photoexcitation wavelength of 650 nm and a pump fluence of 10 μJ·cm^{-2}, (d-f) Transient band edge bleach decay kinetics (probed at 725 nm) and corresponding tri-exponential fitting curves for HTL/PVK, HTL/2PACz/PVK, and HTL/MeO-2PACz/PVK, respectively, at different pump fluences of 10^{-1} μJ·cm^{-2}.

corresponds to carrier trapping processes at the HTL/PVK interface, and the observed faster trap filling at the interface by employing MeO-2PACz as a SAM interlayer suggests large quasi-fermi-level splitting and is accountable for V_{oc} enhancement [59]. The τ_2 component in the fs-TAS decay dynamics corresponds to the hole transport rate in the HTL/PVK system. The extracted τ_2 component (Table S3) at different pump fluences are 412 ps (8%), 319 ps (32%), and 158 ps (42%) for HTL/PVK, 260 ps (22%), 195 ps (48%), and 144 ps (46%) for HTL/2PACz/PVK, and 221 ps (20%), 147 ps (43%), and 125 ps (48%) for HTL/MeO-2PACz/PVK film. The fast decay observed for τ_2 in the HTL/MeO-2PACz/PVK structure suggests an improved hole transport process, which aligns well with the UPS and PLQE results as discussed earlier. Moreover, at the HTL/PVK interface, the hole injection rate improved due to a slight increase in the WF. Organic molecules or SAMs with a permanent dipole moment can effectively tune the WF, thereby enhancing the hole extraction process [60–62]. Additionally, the long-lived component τ_3 is associated with exciton recombination within the bulk of PVK and at the grain boundaries [50]. Since our focus was on observing hole carrier dynamics, we performed fs-TAS measurements, and the exciton recombination decay kinetics, which occur in the ps-ns range, are beyond the detection limits of fs-TAS.

Based on the above findings, the plausible schematic representation is depicted in Fig. 5. Bulk defects that are clearly visible HTL/PVK film might originate from the highly acidic character and hydrophilicity of PEDOT:PSS. This may hamper Sn-PVK film as observed through TAS analysis where shifts in the density of states are visible at different delay times. This might be originating from the formation of new sub-band states and resulted in the renormalization of the bandgap. Moreover, a slight reduction in the trap density states was observed in HTL/2PACz/PVK. It is speculated that the buried interface chemically interacts with the beneath PEDOT:PSS layer and suppresses direct contact of PEDOT:PSS with PVK. Based on the observations in the present study, we analyzed that MeO-2PACz at the buried interface interacts with PEDOT:PSS through the anchoring of the phosphonic group, and the methoxy terminal group chemically interacts with Sn-PVK, thereby controlling the bulk defect states in PVK. The SS-PL analysis shows PL quenching efficiency increases in HTL/MeO-2PACz/PVK as compared to the rest of the cases which is further testified through the TAS analysis in which the photoinduced transient bleach shows constant band states after initial renormalization, which appears due to the passivation of defects in HTL/MeO-2PACz/PVK. In addition, we speculate that the chemical interactions of the SAM interlayer with PEDOT:PSS lead to a slight improvement in the work function. Through the TAS and UPS study, we predict that HTL/MeO-2PACz/PVK has comparatively improved work function with better hole transport rate (TAS) as shown in the band energy diagram in Fig. 5(b). These factors collectively contribute to the improved V_{oc} in the HTL/MeO-2PACz/PVK device. To demonstrate the impact of the SAM interlayer on device stability and validate the observations, stability testing was conducted for each device (Fig. 5 (c, d)). In Fig. 5(c), the stability tests revealed that the HTL/MeO-2PACz/PVK device retained nearly 100% of its initial PCE after 2000 hrs under N_2 atmospheric conditions. In contrast, the HTL/2PACz/PVK and HTL/PVK devices retained only 80% and 60% of their original PCE, respectively. Subsequently, aging tests were performed under ambient air conditions (Fig. 5(d)), and the HTL/MeO-2PACz/PVK device exhibited better stability by maintaining 92.6% of initial PCE. Figure S19 provides monitored images of the HTL/PVK, HTL/2PACz/PVK, and HTL/MeO-2PACz/PVK films at different time intervals. Based on the detailed analysis, it can be concluded that the insertion of MeO-2PACz SAM, with anchoring and terminal groups, promotes greater compactness at the HTL/Sn-PVK interface. This compactness also contributes to the reduction of defects within the bulk of the PVK layer. As a result, the various benefits obtained from the MeO-2PACz interlayer collectively enhance device performance and stability. These findings suggest a promising avenue

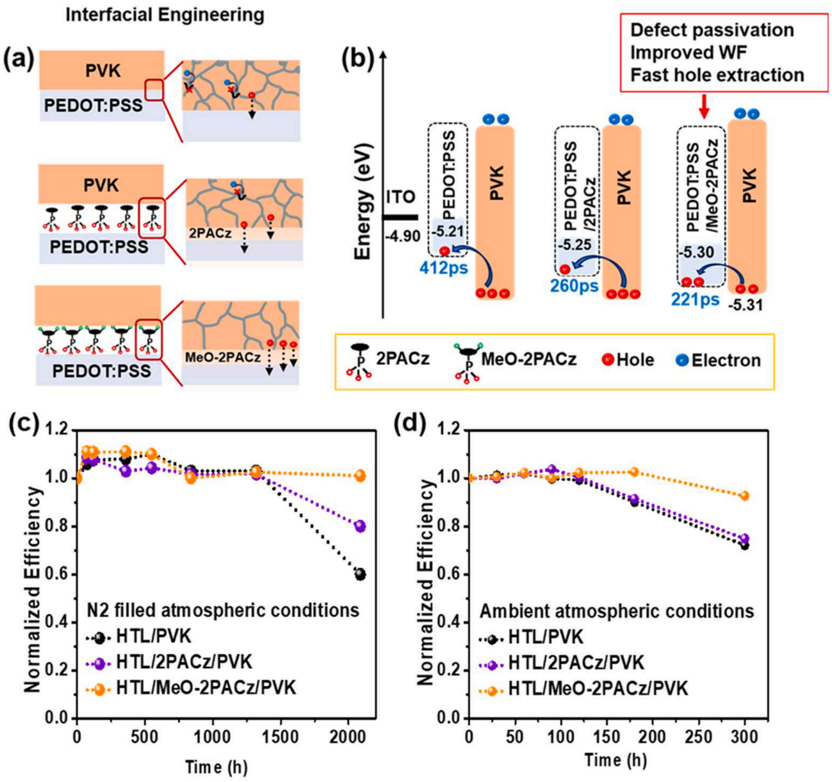

Fig. 5. Interfacial engineering: (a) Self-assembled monolayer (SAM) between PEDOT:PSS (HTL)-Perovskite (PVK) layer, anchoring group interaction with PEDOT:PSS and terminal group (methoxy) of MeO-2PACz interaction with perovskite helps in perovskite defect passivation. (b) Change in work function and energy band alignment of PEDOT:PSS/PVK, PEDOT:PSS/2PACz/PVK, and PEDOT:PSS/MeO-2PACz/PVK. Long-term stability tests of WBG Sn-PSCs with various interfacial SAM treatments under (c) N_2 atmospheric condition for > 2000 h, (d) ambient air (i.e., under 25 °C, R.H. of 30–50%) for 300 h without encapsulation.

for interfacial engineering in the further developments of WBG Sn-PSCs and future Pb-free all-PVK tandem cells.

3. Conclusion

In summary, the utilization of MeO-2PACz SAM with anchoring and terminal groups at PEDOT:PSS HTL/Sn-PVK interface offers significant advantages over 2PACz. This approach led to the accomplishment of a record PCE of 12.16% (with a certified PCE of 11.60%) in WBG (>1.65 eV) Sn-PSC to date. Chemical analysis revealed that the interaction between P-O^{-} of 2PACz/MeO-2PACz (deprotonation of the phosphonic acid group) and S^{+} (PEDOT: PSS) at PEDOT:PSS/SAM interface led to an improved work function. NMR spectroscopy demonstrated that the interaction between the terminal methoxy O^{-} donor (MeO-2PACz) and the Sn octahedral (perovskite) at the SAM/PVK interface significantly reduced trap densities. Moreover, the PIB bands observed in fs-TAS exhibited negligible band shift (HTL/MeO-2PACz/PVK) within a delay time range of 100–1000 ps, indicating an enhancement in V_{oc}. The higher PLQE of 47% for HTL/MeO-2PACz/PVK and the reduced relaxation kinetics of τ_1 from 26 ps (HTL/PVK) to 19 ps for HTL/MeO-2PACz/PVK suggests rapid trap filling at the interface. Additionally, the τ_2 component, which represents hole extraction, decreased from 158 ps (HTL/PVK) to 125 ps for HTL/MeO-2PACz/PVK, indicating improved hole extraction efficiency. Interfacial engineering with MeO-2PACz successfully increased the film crystallinity of the PVK layer with the preferred orientation. These findings strongly suggest that interfacial engineering with MeO-2PACz in WBG Sn-PSCs can effectively passivate PVK defects, enhance hole transport characteristics, and improve device stability. This study provides crucial insights into controlling the HTL/Sn-PVK interface using SAMs for the development of high-efficiency, lead-free single-junction, and future tandem solar cells.

4. Experimental section

4.1. Materials

Indium tin oxide (ITO)-coated glass substrates (AMG, 10 Ω sq^{-1}), acetone (~99%) and isopropanol (IPA, ~ 99.5%) (For substrate cleaning and IPA as SAM solvent), DMF (99.5%), DMSO (99.8%) (perovskite precursor solvents), Toluene (99.8%) (antisolvent), Dichlorobenzene (99.0%) purchased from Samchun Chemical and chlorobenzene (99% - GR grade, Wako) were used as ETL solvents. Precursor salts i.e., Formamidinium bromide (FABr), Methylammonium bromide (MABr), Phenylethyl ammonium bromide (PEABr) purchased from greatcellsolar, Tin (II) Iodide (SnI_2, Alfa Aesar) and Tin (II) fluoride (SnF_2, sigma-aldrich) used without further purification. PEDOT: PSS procured from Heraeus, Germany used as HTL, [2-(9H-carbazol-9-yl)ethyl] phosphonic acid (2PACz) and [2-(3,6-dimethoxy-9H-carbazol-9-yl) ethyl] phosphonic acid (MeO-2PACz) (self-assembled monolayers procured from TCI), Phenyl-C61-butyric acid methyl ester (PCBM, 99.5%, Organic Semiconductor Materials, Republic of Korea) and Bathocuproin (BCP, 99.9%, Alfa Aesar) were used as electron transport layers (ETL). Perovskite ($PEA_{0.15}FA_{0.75}MA_{0.10}SnI_2Br$ (PVK)) precursor solution preparation is the same as reported in our previous research article [6].

$PEA_{0.15}FA_{0.75}MA_{0.10}SnI_2Br$ perovskite solution was prepared by first dissolving PEABr (30.3 mg), SnI_2 (372.52 mg), SnF_2 (15.67 mg), FABr (93.7 mg), Sn (sufficient amount), MABr (11.2 mg) in DMF: DMSO (4:1). Perovskite precursor solution stirred at 60 °C for 2 h 30 min inside N_2 filled glove box (GB). 2PACz and MeO-2PACz SAM solutions were prepared in IPA with a molar concentration of 0.40 mg mL^{-1}. PCBM solution was prepared with 20 mg mL^{-1} in mixed solvent chlorobenzene: dichlorobenzene in 1:1 ratio and kept for overnight stirring at room temperature (RT).

4.2. Perovskite solar cell fabrication procedure

ITO-substrates cleaned with acetone in the ultrasonic bath for 15 min followed by cleaning substrates in IPA. Substrates were dried in oven for 10 min at 95 °C to evaporate solvents. Cleaned ITO substrates were UV-Ozone treated for 20 min. At initial step PEDOT: PSS (HTL) coated on substrates at 5000 rpm for 30 s in ambient atmospheric conditions and annealed at 150 °C (20 min) on hotplate. For HTL/2PACz/PVK and HTL/MeO-2PACz/PVK PSC fabrication additional step needs to be followed before perovskite coating on top of HTL. In which 80 μL 2PACz or MeO-2PACz (solution in IPA) coated over PEDOT:PSS through dynamic coating spined at 3000 rpm for 30 s. further substrates get heated at 100 °C for 10 min. Washing out excess SAM molecules is essential for efficient devices hence HTL/SAM coated substrates washed with 80 μL IPA (dynamic coating) and heated for 1 min to remove any traces of solvent. Later, HTL/SAM coated substrates transferred inside a N_2 filled glove box prior perovskite coating. The perovskite films prepared by spin coating filtered perovskite precursor solution at 8000 rpm for 30 s, followed with antisolvent dripping (200 μL Toluene) at 10th *sec* on perovskite film. These perovskite films further annealed at 70 °C for 10 min on hot plate for perovskite crystallization. In next step electron transport layer (ETL) PCBM spin-coated onto the perovskite film at 1500 rpm for 30 s and annealed at 70 °C for 10 min, followed with BCP solution coating with 0.5 mg mL^{-1} in IPA solution coated dynamically over PCBM layer at 6000 rpm for 30 s annealed for 5 mins at 70 °C on hot plate. Silver electrodes deposited through thermal evaporator under a high vacuum condition ($\sim 3 \times 10^{-6}$ Torr).

4.3. Characterizations

The short current density-open circuit voltage (J_{sc}-V_{oc}) characteristic curves of p-i-n wide bandgap Sn perovskite solar cells were measured through solar simulator (PEC-L01, Peccell Technologies) under standard air mass (AM) 1.5 illumination (1000 W/m^2 light intensity) in ambient atmospheric conditions with the scan rate of 250 mV/s (effective cell area 0.04 cm^2).

EQE measurement was carried out using a power source (Abet Technologies 150 W xenon lamp, 13,014) with monochromator (DongWoo Optron, MonoRa500i) assembled with Compact Stat instrument (Ivium Technologies; Eindhoven, The Netherlands). EIS study was performed by applying 0.65 V under dark conditions at same instrument in the frequency ranges of 2 MHz to 100 Hz. Notably, all device characterization was carried out in ambient atmospheric conditions (i. e., under 25 °C, R.H. of 30–50 %). TPV and TPC measurements were carried out with an organic semiconductor parameter system (T400, Mcscience) comprising of a Tektronix oscilloscope (DPO-2014B) 100 MHz bandwidth. Carrier lifetime and extraction time calculated through biexponentially fitting the data applying following equation.

$$V_{oc} \ or \ J_{sc} = A1 \ exp(-t/\tau_1) + A2 \ exp(-t/\tau_2) \quad (1)$$

C-V (M-S curve) response of PSCs to evaluate the trap density. Frequency of 1000 Hz and AC voltage of 0.01 V were filled in the initial and final conditions. Then the applied direct current (DC) voltage was set in the range from −0.2 to 1.0 V (forward bias) with 25 mV steps and devices were measured under dark conditions.

Perovskite crystallinity preferential orientation and phase purity was detected through XRD, D8-Advance, Bruker-AXS diffracted beam monochromator was equipped in the X-ray diffractometer (Cu K_{α} radiation, $\lambda = 1.541$ Å) and 2D GIWAXS. 2D GIWAXS measurements was carried out at 9A U-SAXS beamline (Pohang Accelerator Laboratory in Korea). Patterns were recorded with a 2D charge coupled detector (MX170-HS, Rayonix Ltd.), where X-ray wavelength and sample-to-detector (SDD) were fixed to 0.626 Å and 221 mm. Diffraction angle was calibrated with pre-calibrated sucrose (Monoclinic, P21, a = 10.8631 Å, b = 8.7044 Å, c = 7.7624 Å and β = 102.938°). Film morphology was observed by FE-SEM; SIGMA, Carl Zeiss. XPS and UPS

(XPS-Theta Probe) measurement was conducted using K-Alpha$^+$ system (Thermo Fisher Scientific) with monochromatic Al Kα X-ray radiation (1486.6 eV). The work function (ϕ) was calculated through UPS data.

The steady-state fluorescence spectra were recorded using a Hitachi F-7000 fluorescence spectrophotometer. fs-TAS and decays were recorded using a homemade TA spectrometer combined with a femtosecond Ti:sapphire regenerative amplifier system (Hurricane, Spectra Physics). A pump pulse at 650 nm with a power density of 1~10 μJ/cm^2 was produced using an optical parametric amplifier (IR-OPA, Spectra Physics) and a neutral density filter, while a broadband white-light continuum probe pulse was generated by focusing a small portion of the 800 nm amplifier output into a sapphire window. TA signals in respective optical delays of pump and probe pulses were collected using an optical fiber coupled with multichannel spectrometers from Ocean Insight (Ocean FX). More details on this system were noted in the previous publication [63,64].

NMR measurement details: ^{13}C NMR spectra of the 2PACz, 2PACz·SnI$_2$, MeO-2PACz and MeO-2PACz·SnI$_2$ samples were recorded by using a 600 MHz Varian NMR spectrometer (VNS-600, Agilent, Palo Alto, CA, USA). The samples were dispersed in DMSO-d6 solvent (concentration = 1 mL) and filled into the NMR tube for measurement. 2PACz (30 mg/ml), 2PACz·SnI$_2$ (2PACz: SnI$_2$ = 30 mg/ml: 30 mg/ml), MeO-2PACz (30 mg/ml), MeO-2PACz·SnI$_2$ (MeO-2PACz: SnI$_2$ = 30 mg/ml: 30 mg/ml).

Supporting information

Comparative analysis data and tables: PSCs statistical data, EQE, FESEM, SS-PL, UPS, XPS, and NMR measurement.

CRediT authorship contribution statement

SungWon Cho: Conceptualization, Methodology, Writing – original draft. **Padmini Pandey:** Investigation, Methodology, Writing – original draft. **Saemon Yoon:** Data curation, Software. **Jun Ryu:** Data curation, Software. **Dong-Gun Lee:** Formal analysis, Investigation. **Qing Shen:** Investigation, Writing – review & editing. **Shuzi Hayase:** Resources, Writing – review & editing. **Hochan Song:** Formal analysis, Investigation. **Hyosung Choi:** Methodology, Writing – review & editing. **Hyungju Ahn:** Resources, Visualization. **Chang-Mok Oh:** Validation, Visualization. **In-Wook Hwang:** Validation, Visualization. **Jung Sang Cho:** Funding acquisition, Supervision, Writing – review & editing. **Dong-Won Kang:** Conceptualization, Funding acquisition, Project administration, Supervision.

Declaration of Competing Interest

The authors declare that they have no known competing financial interests or personal relationships that could have appeared to influence the work reported in this paper.

Data availability

Data will be made available on request.

Acknowledgments

This work was a National Research Foundation of Korea (NRF) grant funded by the Korean government (MSIT) (NRF - 2021R1A2C4002045, 2021R1A4A2001687, RS-2023–00217270, RS-2023-00212744 2023K2A9A2A08000151) and also supported by the GIST Research Institute (GRI) APRI grant funded by the GIST in 2022.

Supplementary materials

Supplementary material associated with this article can be found, in the online version, at doi:10.1016/j.surfin.2023.103478.

References

[1] H. Min, D.Y. Lee, J. Kim, G. Kim, K.S. Lee, J. Kim, M.J. Paik, Y.K. Kim, K.S. Kim, M. G. Kim, Perovskite solar cells with atomically coherent interlayers on SnO$_2$ electrodes, Nature 598 (7881) (2021) 444–450, https://doi.org/10.1038/s41586-021-03964-8.

[2] R. He, S. Ren, C. Chen, Z. Yi, Y. Luo, H. Lai, W. Wang, G. Zeng, X. Hao, Y. Wang, Wide-bandgap organic–inorganic hybrid and all-inorganic perovskite solar cells and their application in all-perovskite tandem solar cells, Energy Environ. Sci. 14 (11) (2021) 5723–5759, https://doi.org/10.1039/D1EE01562A.

[3] A. Mallick, I. Visoly-Fisher, Pb in halide perovskites for photovoltaics: reasons for optimism, Mater. Adv. 2 (2021) 6125–6135, https://doi.org/10.1039/D1MA00355K.

[4] B.B. Yu, Z. Chen, Y. Zhu, Y. Wang, B. Han, G. Chen, X. Zhang, Z. Du, Z. He, Heterogeneous 2D/3D tin-halides perovskite solar cells with certified conversion efficiency breaking 14%, Adv. Mater. 33 (36) (2021), 2102055.

[5] P. Pandey, S. Cho, S. Hayase, J.S. Cho, D.W. Kang, New strategies to develop high-efficiency lead-free wide bandgap perovskite solar cells, Chem. Eng. J. 448 (2022), 137622, https://doi.org/10.1016/j.cej.2022.137622.

[6] S. Cho, P. Pandey, J. Park, T.W. Lee, H. Ahn, H. Choi, D.W. Kang, Phenylethylammonium-formamidinium-methylammonium quasi-2D/3D tin wide-bandgap perovskite solar cell with improved efficiency and stability, Chem. Eng. J. 446 (Part 4) (2022), 137388, https://doi.org/10.1016/j.cej.2022.137388.

[7] J.J. Cao, Y.H. Lou, W.F. Yang, K.L. Wang, Z.H. Su, J. Chen, C.H. Chen, C. Dong, X. Y. Gao, Z.K. Wang, Multifunctional potassium thiocyanate interlayer for eco-friendly tin perovskite indoor and outdoor photovoltaics, Chem. Eng. J. 433 (2022), 133832, https://doi.org/10.1016/j.cej.2021.133832.

[8] M. Chen, G. Kapil, L. Wang, S.R. Sahamir, A.K. Baranwal, K. Nishimura, Y. Sanehira, Z. Zhang, M.A. Kamarudin, Q. Shen, High performance wide bandgap Lead-free perovskite solar cells by monolayer engineering, Chem. Eng. J. 436 (2022), 135196, https://doi.org/10.1016/j.cej.2022.135196.

[9] T.Y. Teng, F. Hu, Y.H. Lou, J.J. Cao, C.H. Chen, Y.R. Shi, K.L. Wang, J. Chen, Z. K. Wang, L.S. Liao, Repaired surface structural imperfection of tin wide-bandgap perovskite films for photovoltaic application, Chem. Eng. J. 457 (2023), 141292, https://doi.org/10.1016/j.cej.2023.141292.

[10] F. Hu, C.H. Chen, Y.H. Lou, T.Y. Teng, Y.R. Shi, Y. Xia, K.L. Wang, J. Chen, Z. K. Wang, L.S. Liao, A vertical antioxidant strategy for high performance wide band gap tin perovskite photovoltaics, J. Mater. Chem. A 11 (9) (2023) 4579–4586, https://doi.org/10.1039/D2TA09363D.

[11] W. Han, G. Ren, J. Liu, Z. Li, H. Bao, C. Liu, W. Guo, Recent progress of inverted perovskite solar cells with a modified PEDOT: PSS hole transport layer, ACS Appl. Mater. Interfaces 12 (44) (2020) 49297–49322, https://doi.org/10.1021/acsami.0c13576.

[12] Y. Lin, A. Magomedov, Y. Firdaus, D. Kaltsas, A. El-Labban, H. Faber, D. R. Naphade, E. Yengel, X. Zheng, E. Yarali, 18.4% organic solar cells using a high ionization energy self-assembled monolayer as hole-extraction interlayer, ChemSusChem 14 (17) (2021) 3569–3578, https://doi.org/10.1002/cssc.202100707.

[13] N. Sun, W. Gao, H. Dong, Y. Liu, X. Liu, Z. Wu, L. Song, C. Ran, Y. Chen, Architecture of pin Sn-based perovskite solar cells: characteristics, advances, and perspectives, ACS Energy Lett 6 (8) (2021) 2863–2875, https://doi.org/10.1021/acsenergylett.1c01170.

[14] S.Y. Kim, S.J. Cho, S.E. Byeon, X. He, H.J. Yoon, Self-assembled monolayers as interface engineering nanomaterials in perovskite solar cells, Adv. Energy Mater. 10 (44) (2020), https://doi.org/10.1002/aenm.202002606, 2002606.

[15] Y. Wang, Q. Liao, J. Chen, W. Huang, X. Zhuang, Y. Tang, B. Li, X. Yao, X. Feng, X. Zhang, Teaching an old anchoring group new tricks: enabling low-cost, eco-friendly hole-transporting materials for efficient and stable perovskite solar cells, J. Am. Chem. Soc. 142 (39) (2020) 16632–16643.

[16] Q. Liao, Y. Wang, Z. Zhang, K. Yang, Y. Shi, K. Feng, B. Li, J. Huang, P. Gao, X. Guo, Self-assembled donor-acceptor hole contacts for inverted perovskite solar cells with an efficiency approaching 22%: the impact of anchoring groups, J. Energy Chem. 68 (2022) 87–95.

[17] L. Chu, L. Ding, Self-assembled monolayers in perovskite solar cells, J. Semiconduct. 42 (9) (2021), 090202–090202-3.

[18] A. Al-Ashouri, A. Magomedov, M. Roß, M. Jošt, M. Talaikis, G. Chistiakova, T. Bertram, J.A. Márquez, E. Köhnen, E. Kasparavičius, Conformal monolayer contacts with lossless interfaces for perovskite single junction and monolithic tandem solar cells, Energy Environ. Sci. 12 (11) (2019) 3356–3369, https://doi.org/10.1039/C9EE02268F.

[19] Q. Wang, C.C. Chueh, T. Zhao, J. Cheng, M. Eslamian, W.C. Choy, A.K.Y. Jen, Effects of self-assembled monolayer modification of nickel oxide nanoparticles layer on the performance and application of inverted perovskite solar cells, ChemSusChem 10 (19) (2017) 3794–3803, https://doi.org/10.1002/cssc.201701262.

[20] M.Y. Zhu, L.X. Zhang, J. Yin, J.J. Chen, L.J. Bie, Ppt-level benzene detection and gas sensing mechanism using (C$_4$H$_9$NH$_3$)$_2$PbI$_2$Br$_2$ organic–inorganic layered perovskite, Inorg. Chem. Front. 5 (12) (2018) 3046–3052, https://doi.org/10.1039/C8QI00803E.

[21] S. Shao, J. Liu, G. Portale, H.H. Fang, G.R. Blake, G.H. ten Brink, L.J.A. Koster, M. A. Loi, Highly reproducible Sn-based hybrid perovskite solar cells with 9% efficiency, Adv. Energy Mater. 8 (4) (2018), 1702019, https://doi.org/10.1002/aenm.201702019.

[22] S. Xiong, Z. Hou, S. Zou, X. Lu, J. Yang, T. Hao, Z. Zhou, J. Xu, Y. Zeng, W. Xiao, Direct observation on p-to n-type transformation of perovskite surface region during defect passivation driving high photovoltaic efficiency, Joule 5 (2) (2021) 467–480, https://doi.org/10.1016/j.joule.2020.12.009.

[23] L. Liu, A. Mei, T. Liu, P. Jiang, Y. Sheng, L. Zhang, H. Han, Fully printable mesoscopic perovskite solar cells with organic silane self-assembled monolayer, J. Am. Chem. Soc. 137 (5) (2015) 1790–1793.

[24] C. Wang, F. Gu, Z. Zhao, H. Rao, Y. Qiu, Z. Cai, G. Zhan, X. Li, B. Sun, X. Yu, Self-repairing tin-based perovskite solar cells with a breakthrough efficiency over 11%, Adv. Mater. 32 (31) (2020), 1907623.

[25] B. Hailegnaw, N.S. Sariciftci, M.C. Scharber, Impedance spectroscopy of perovskite solar cells: studying the dynamics of charge carriers before and after continuous operation, Phys. Status Solidi A 217 (22) (2020), 2000291, https://doi.org/10.1002/pssa.202000291.

[26] X. Deng, F. Qi, F. Li, S. Wu, F.R. Lin, Z. Zhang, Z. Guan, Z. Yang, C.S. Lee, A.K. Y. Jen, Co-assembled monolayers as hole-selective contact for high-performance inverted perovskite solar cells with optimized recombination loss and long-term stability, Angewandte Chemie Int. Ed. 61 (30) (2022), e202203088, https://doi.org/10.1002/anie.202203088.

[27] J. Bahadur, S. Cho, P. Pandey, J. Ryu, S. Yoon, D.G. Lee, J.T. Song, J.S. Cho, D. W. Kang, Surface defect passivation of All-Inorganic $CsPbI_2Br$ perovskites via fluorinated ionic liquid for efficient outdoor/Indoor photovoltaics processed in ambient air, Appl. Surf. Sci. 637 (2023), 157901, https://doi.org/10.1016/j.apsusc.2023.157901.

[28] C. Bi, Q. Wang, Y. Shao, Y. Yuan, Z. Xiao, J. Huang, Non-wetting surface-driven high-aspect-ratio crystalline grain growth for efficient hybrid perovskite solar cells, Nat. Commun. 6 (1) (2015) 1–7, https://doi.org/10.1038/ncomms8747.

[29] J. Zhuang, P. Mao, Y. Luan, X. Yi, Z. Tu, Y. Zhang, Y. Yi, Y. Wei, N. Chen, T. Lin, Interfacial passivation for perovskite solar cells: the effects of the functional group in phenethylammonium iodide, ACS Energy Lett. 4 (12) (2019) 2913–2921, https://doi.org/10.1021/acsenergylett.9b02375.

[30] Y. Zhao, H. Su, Q. Liu, L. Zhang, M. Lv, C. Jiao, P. Cheng, D. Liu, D. He, Improvement of the optoelectrical properties of a transparent conductive polymer via a simple mechanical pressure treatment, ACS Omega 5 (13) (2020) 7545–7554, https://doi.org/10.1021/acsomega.0c00355.

[31] E. Vitoratos, S. Sakkopoulos, E. Dalas, N. Paliatsas, D. Karageorgopoulos, F. Petraki, S. Kennou, S.A. Choulis, Thermal degradation mechanisms of PEDOT: PSS, Org Electron. 10 (1) (2009) 61–66, https://doi.org/10.1016/j.orgel.2008.10.008.

[32] Y.R. Kim, O.J. Sandberg, S. Zeiske, G. Burwell, D.B. Riley, P. Meredith, A. Armin, Mitigating detrimental effect of self-doping near the anode in highly efficient organic solar cells, Adv. Funct. Mater. 33 (16) (2023), 2300147, https://doi.org/10.1002/adfm.202300147.

[33] B. Zhang, T. Kong, W. Xu, R. Su, Y. Gao, G. Cheng, Surface functionalization of zinc oxide by carboxyalkylphosphonic acid self-assembled monolayers, Langmuir 26 (6) (2010) 4514–4522, https://doi.org/10.1021/la9042827.

[34] M. Textor, L. Ruiz, R. Hofer, A. Rossi, K. Feldman, G. Hähner, N.D. Spencer, Structural chemistry of self-assembled monolayers of octadecylphosphoric acid on tantalum oxide surfaces, Langmuir 16 (7) (2000) 3257–3271, https://doi.org/10.1021/la990941t.

[35] Y. Lin, Y. Firdaus, F.H. Isikgor, M.I. Nugraha, E. Yengel, G.T. Harrison, R. Hallani, A. El-Labban, H. Faber, C. Ma, Self-assembled monolayer enables hole transport layer-free organic solar cells with 18% efficiency and improved operational stability, ACS Energy Lett 5 (9) (2020) 2935–2944, https://doi.org/10.1021/acsenergylett.0c01421.

[36] C. Rocks, V. Svrcek, P. Maguire, D. Mariotti, Understanding surface chemistry during $MAPbI_3$ spray deposition and its effect on photovoltaic performance, J. Mater. Chem. C 5 (4) (2017) 902–916, https://doi.org/10.1039/C6TC04864A.

[37] Q. Zhou, L. Liang, J. Hu, B. Cao, L. Yang, T. Wu, X. Li, B. Zhang, P. Gao, High-performance perovskite solar cells with enhanced environmental stability based on a $(p\text{-}FC_6H_4C_2H_4NH_3)_2[PbI_4]$ capping layer, Adv. Energy Mater. 9 (12) (2019), 1802595, https://doi.org/10.1002/aenm.201802595.

[38] H. Park, S.H. Lee, F.S. Kim, H.H. Choi, I.W. Cheong, J.H. Kim, Enhanced thermoelectric properties of PEDOT: PSS nanofilms by a chemical dedoping process, J. Mater. Chem. A 2 (18) (2014) 6532–6539, https://doi.org/10.1039/C3TA14960A.

[39] M.C. Tang, S. Zhang, T.J. Magnanelli, N.V. Nguyen, E.J. Heilweil, T. D. Anthopoulos, C.A. Hacker, Unraveling the compositional heterogeneity and carrier dynamics of alkali cation doped 3D/2D perovskites with improved stability, Mater. Adv. 2 (4) (2021) 1253–1262, https://doi.org/10.1039/D0MA00967A.

[40] J. Chen, X. Zhao, Y. Cheng, J. Qian, M. Wang, W. Shen, K. Cao, Y. Huang, W. Hui, Y. Gu, hydroxyl-rich d-sorbitol to address transport layer/perovskite interfacial issues toward highly efficient and stable 2D/3D tin-based perovskite solar cells, Adv. Opt. Mater. 9 (22) (2021), 2100755, https://doi.org/10.1002/adom.202100755.

[41] P. Li, H. Dong, J. Xu, J. Chen, B. Jiao, X. Hou, J. Li, Z. Wu, Ligand orientation-induced lattice robustness for highly efficient and stable tin-based perovskite solar cells, ACS Energy Lett. 5 (7) (2020) 2327–2334, https://doi.org/10.1021/acsenergylett.0c00960.

[42] S. Ning, S. Zhang, J. Sun, C. Li, J. Zheng, Y.M. Khalifa, S. Zhou, J. Cao, Y. Wu, Ambient pressure X-ray photoelectron spectroscopy investigation of thermally stable halide perovskite solar cells via post-treatment, ACS Appl. Mater. Interfaces 12 (39) (2020) 43705–43713, https://doi.org/10.1021/acsami.0c12044.

[43] Z. Guo, X. Xue, X. Sun, D. Li, F. Wang, L. Fan, X. Liu, L. Yang, M. Wei, Activate whole-body passivation ability of small isomeric D-π-A molecules via amino position effect to improve the photovoltaic performance of perovskite solar cells, Chem. Eng. J. 452 (Part2) (2023), 139321, https://doi.org/10.1016/j.cej.2022.139321.

[44] G.R. Fulmer, A.J. Miller, N.H. Sherden, H.E. Gottlieb, A. Nudelman, B.M. Stoltz, J. E. Bercaw, K.I. Goldberg, NMR chemical shifts of trace impurities: common laboratory solvents, organics, and gases in deuterated solvents relevant to the organometallic chemist, Organometallics 29 (9) (2010) 2176–2179, https://doi.org/10.1021/om100106e.

[45] F. Yuan, X. Zheng, A. Johnston, Y.K. Wang, C. Zhou, Y. Dong, B. Chen, H. Chen, J. Z. Fan, G. Sharma, Color-pure red light-emitting diodes based on two-dimensional lead-free perovskites, Sci. Adv. 6 (42) (2020) eabb0253, https://doi.org/10.1126/sciadv.abb0253.

[46] X. Zhou, J. Qiu, J. Li, W. Qi, Y. Li, S. Jiao, H. Ling, P. Wang, F. Liu, K. Sohail, Reduced defects and enhanced Vbi in perovskite absorbers through synergetic passivating effect using 4-methoxyphenylacetic acid, J. Power Sources 518 (2022), 230734, https://doi.org/10.1016/j.jpowsour.2021.230734.

[47] M. Abdi-Jalebi, M.I. Dar, S.P. Senanayak, A. Sadhanala, Z. Andaji-Garmaroudi, L. M. Pazos-Outón, J.M. Richter, A.J. Pearson, H. Sirringhaus, M. Grätzel, Charge extraction via graded doping of hole transport layers gives highly luminescent and stable metal halide perovskite devices, Sci. Adv. 5 (2) (2019) eaav2012, https://doi.org/10.1126/sciadv.aav2012.

[48] X. Liu, T. Wu, C. Zhang, Y. Zhang, H. Segawa, L. Han, Interface energy-level management toward efficient tin perovskite solar cells with hole-transport-layer-free structure, Adv. Funct. Mater. 31 (50) (2021), 2106560, https://doi.org/10.1002/adfm.202106560.

[49] H. Choi, C.K. Mai, H.B. Kim, J. Jeong, S. Song, G.C. Bazan, J.Y. Kim, A.J. Heeger, Conjugated polyelectrolyte hole transport layer for inverted-type perovskite solar cells, Nat. Commun. 6 (1) (2015) 1–6, https://doi.org/10.1038/ncomms8348.

[50] J.I. Khan, F.H. Isikgor, E. Ugur, W. Raja, G.T. Harrison, E. Yengel, T. D. Anthopoulos, S. De Wolf, F. Laquai, Charge carrier recombination at perovskite/hole transport layer interfaces monitored by time-resolved spectroscopy, ACS Energy Lett. 6 (12) (2021) 4155–4164, https://doi.org/10.1021/acsenergylett.1c01931.

[51] J.T. DuBose, P.V. Kamat, Hole trapping in halide perovskites induces phase segregation, Acc. Mater. Res. 3 (7) (2022) 761–771, https://doi.org/10.1021/accountsmr.2c00076.

[52] J. Kim, R. Godin, S.D. Dimitrov, T. Du, D. Bryant, M.A. McLachlan, J.R. Durrant, Excitation density dependent photoluminescence quenching and charge transfer efficiencies in hybrid perovskite/organic semiconductor bilayers, Adv. Energy Mater. 8 (35) (2018), 1802474, https://doi.org/10.1002/aenm.201802474.

[53] S. Narra, E. Jokar, O. Pearce, C.Y. Lin, A. Fathi, E.W.G. Diau, Femtosecond transient absorption spectra and dynamics of carrier relaxation of tin perovskites in the absence and presence of additives, J. Phys. Chem. Lett. 11 (14) (2020) 5699–5704, https://doi.org/10.1021/acs.jpclett.0c01589.

[54] J. Horn, I. Minda, H. Schwoerer, D. Schlettwein, Direct observation of charge injection from $CH_3NH_3PbI_{3-x}Cl_x$ to organic semiconductors monitored with sub-ps transient absorption spectroscopy, Phys. Status Solidi B 256 (3) (2019), 1800265, https://doi.org/10.1002/pssb.201800265.

[55] Z. Zhu, J. Ma, Z. Wang, C. Mu, Z. Fan, L. Du, Y. Bai, L. Fan, H. Yan, D.L. Phillips, Efficiency enhancement of perovskite solar cells through fast electron extraction: the role of graphene quantum dots, J. Am. Chem. Soc. 136 (10) (2014) 3760–3763, https://doi.org/10.1021/ja4132246.

[56] M.B. Price, J. Butkus, T.C. Jellicoe, A. Sadhanala, A. Briane, J.E. Halpert, K. Broch, J.M. Hodgkiss, R.H. Friend, F. Deschler, Hot-carrier cooling and photoinduced refractive index changes in organic–inorganic lead halide perovskites, Nat. Commun. 6 (1) (2015) 1–8, https://doi.org/10.1038/ncomms9420.

[57] Y. Yang, D.P. Ostrowski, R.M. France, K. Zhu, J. Van De Lagemaat, J.M. Luther, M. C. Beard, Observation of a hot-phonon bottleneck in lead-iodide perovskites, Nat. Photonics 10 (1) (2016) 53–59, https://doi.org/10.1038/nphoton.2015.213.

[58] X. Zhu, C.F.J. Lau, K. Mo, S. Cheng, Y. Xu, R. Li, C. Wang, Q. Zheng, Y. Liu, T. Wang, Inverted planar heterojunction perovskite solar cells with high ultraviolet stability, Nano Energy 103 (2022), 107849, https://doi.org/10.1016/j.nanoen.2022.107849.

[59] E. Serpetzoglou, I. Konidakis, G. Kakavelakis, T. Maksudov, E. Kymakis, E. Stratakis, Improved carrier transport in perovskite solar cells probed by femtosecond transient absorption spectroscopy, ACS Appl. Mater. Interfaces 9 (50) (2017) 43910–43919, https://doi.org/10.1021/acsami.7b15195.

[60] S. Khodabakhsh, B.M. Sanderson, J. Nelson, T.S. Jones, Using self-assembling dipole molecules to improve charge collection in molecular solar cells, Adv. Funct. Mater. 16 (1) (2006) 95–100, https://doi.org/10.1002/adfm.200500207.

[61] H.L. Yip, S.K. Hau, N.S. Baek, H. Ma, A.K.Y. Jen, Polymer solar cells that use self-assembled-monolayer-modified ZnO/metals as cathodes, Adv. Mater. 20 (12) (2008) 2376–2382, https://doi.org/10.1002/adma.200703050.

[62] J.S. Kim, J.H. Park, J.H. Lee, J. Jo, D.Y. Kim, K. Cho, Control of the electrode work function and active layer morphology via surface modification of indium tin oxide for high efficiency organic photovoltaics, Appl. Phys. Lett. 91 (11) (2007), 112111, https://doi.org/10.1063/1.2778548.

[63] C.M. Oh, J. Lee, S.H. Park, I.W. Hwang, Enhanced charge separation in ternary bulk-heterojunction organic solar cells by fullerenes, J. Phys. Chem. Lett. 12 (27) (2021) 6418–6424, https://doi.org/10.1021/acs.jpclett.1c01496.

[64] C.M. Oh, J. Lee, S.H. Park, I.W. Hwang, Carrier losses in non-geminate charge-transferred states of nonfullerene acceptor-based organic solar cells, Spectrochim.

Acta Part A Molecul. Biomolecul. Spectrosc. 250 (2021), 119227, https://doi.org/10.1016/j.saa.2020.119227.